



ORIGINAL RESEARCH ARTICLE

# Developing the Additive Manufacturing Chain of AlSi7Mg with Laser Powder Bed Fusion and Tailored Heat Treatments for Railway Spare Parts

Oriana Tassa, Alessandro Colaneri, Leonardo Fransesini, Federica Sammartino, and Ali Gökhan Demir

Submitted: 6 July 2023 / Accepted: 20 October 2023

The use of metal additive manufacturing technologies in railways sector can provide increased flexibility in terms of spare part logistics. Combined with lightweight metals such as Al-alloys, the product performance can also be enhanced in terms of weight reduction, vibration and noise control. The railway sector is more likely to exploit large and bulky parts produced by laser powder bed fusion (LPBF), which should have appropriate mechanical properties. Therefore, the whole production chain should be analyzed considering the heat treatment steps suited for a distributed and resource efficient manufacturing scheme. Accordingly, this work analyzes the additive manufacturing of AlSi7Mg alloy by LPBF and its consecutive heat treatment steps. In particular, the impact of LPBF process productivity, heat treatment type and atmosphere composition were considered to analyze the most appropriate route for the needs of the railways applications. The results show that with an appropriate direct aging treatment in air, mechanical characteristics of the alloy could be improved, despite that the high layer thickness used in LPBF could increase process productivity. The absence of a quenching step was found to be favorable for large parts, while the absence of an inert gas such as Ar in the heat treatment did not generate any reduction in the mechanical properties.

**Keywords** additive manufacturing logistics, laser powder bed fusion, lightweight design, parts on demand

## 1. Introduction

The well-known and recognized production capabilities of additive manufacturing (AM) techniques can be applied to a wide range of industrial sectors, one of which is the railway industry. In the railways sector a key need regards the supply of spare and discontinued parts (Ref 1). Often such components are stored with quantities to match the possible requirements of up to 30 years. Indeed, such conditions are far from optimal in terms of resource usage. Once the spare part is required, it should be often shipped from centralized warehouses and assembled in the required location. When spare parts are finished or discontinued, they are often produced on demand requiring long lead times. Trains are often used for a long duration of time reaching decades. Indeed, designs and materials used in this timeframe can be improved. The usage of stocked spare parts renders also such possibilities to be limited. A decentralized and in-demand manufacturing of spare parts can be made possible through additive manufacturing processes (Ref 2). In particular, metallic components with small

to medium sizes can be produced locally using digital files and powder feedstock using laser powder bed fusion (LPBF) (Ref 3).

In recent years, the railway industry has started to investigate the use of AM technologies for maintenance purposes (Ref 4, 5). The possibilities also extend toward the use of AM technologies for production of lightweight components (Ref 6, 7). An important point that regards the metal AM processes, in particular LPBF, regards the fact that they are incorporated within a complete manufacturing cycle (Ref 8, 9). Often the LPBF produced parts will require post-processing techniques spanning from heat treatments to surface finishing (Ref 10, 11). For a sustainable decentralized manufacturing of spare parts, the complete manufacturing cycle should be operable in service stations with ease. Hence, beyond the mechanical property requirements, materials that are easier to heat treat are required. From this perspective, Al-alloys present a valid option. Aluminum is a lightweight metal with relatively low melting point (660 °C). The heat treatments are applied intrinsically at temperature ranges (150-400 °C) that require simpler furnaces and low energy consumption (Ref 9). Al-Si-Mg alloy systems are commonly used in LPBF that provide a good balance of processability and mechanical strength (Ref 12). Amongst these alloys some of the most popular ones are AlSi10Mg and AlSi7Mg (Ref 13-17). These alloys processes by LPBF commonly need to undergo stress-relieving and aging treatments. During the LPBF process, the fast cooling rates generate thermal stresses within the material (Ref 18). When the part is released from the base plate, these stresses are relieved by geometrical distortions (Ref 19). A stress-relieving treatment is required before releasing the part from the build plate. While the fast cooling of the LPBF process is highly advantageous for high mechanical strength, the stress relieving

**Oriana Tassa, Alessandro Colaneri, Leonardo Fransesini, and Federica Sammartino**, RINA Consulting – Centro Sviluppo Materiali SpA, Via di Castel Romano 100, 00128 Roma, Italy; and **Ali Gökhan Demir**, Department of Mechanical Engineering, Politecnico di Milano, Via La Masa 1, 20156 Milan, Italy. Contact e-mail: aligokhan.demir@polimi.it.

stage may result in grain coarsening and the agglomeration of the  $Mg_2Si$  phase that results in a lower tensile strength and a higher elongation at rupture (Ref 20). Therefore, an aging treatment accompanies this stage to improve the mechanical strength.

For railways sector, a straightforward and simple heat treatment stage is required. The spare parts to be produced are often bulky fitting into the entire build chamber of commercial systems. Figure 1 shows an example part produced in a  $\phi 300$  mm  $\times$  400 mm build chamber. Such components should be heat-treated without generating distortions throughout the process. From this point, the avoidance of a quenching stage often used in the aging heat treatments is highly favorable. Aging treatments are usually carried out in inert atmosphere. The avoidance of the inert gas can also be beneficial in terms of resource usage.

In the literature, several types of heat treatments have been applied to the AlSi7Mg alloys (Ref 17, 21-26). While most of the works concentrate on the optimum mechanical properties for aerospace and aviation sectors, where the impact of the heat treatment type to its usability in a decentralized production scheme is not of the primary interest. Often these heat treatments are found to be long adding up to the lead times and cost (Ref 27). Concerning the heat treatment atmosphere, while the majority of the works employ inert gases and vacuum environment has also been tested, processing in air appears to be not assessed (Ref 28). Hence, the additive manufacturing cycle planning for applications in decentralized spare part manufacturing remains an open issue. Accordingly, this work studies the LPBF and the successive heat treatment of AlSi7Mg alloy with the aim to provide a feasible recipe for the railways sector by providing a shorter and simpler manufacturing cycle. The LPBF process was studied to ensure high density at different layer thicknesses with the aim to assess the suitability



**Fig. 1** Example of a medium sized component produced by LPBF in AlSi7Mg alloy. The build plate diameter is 300 mm, while the part height is 385 mm

of using higher layer thicknesses to reduce the lead time. Three different heat treatments ranging between conventional T6 to simplified routes have been tested in inert gas and air. The mechanical properties are assessed in the experimented conditions to identify the most suitable route for manufacturing high strength parts.

## 2. Materials and Methods

### 2.1 Powder Feedstock

Gas atomized AlSi7Mg powder with 20-63  $\mu$ m particle diameter range and D50 = 47  $\mu$ m was employed throughout the study (Carpenter Additive, Philadelphia, PA, USA). The nominal chemical composition and the measured one by the powder provider are shown in Table 1, while the SEM image of the powder is shown in Fig. 2. The powder bulk density was 1.24 g/cm<sup>3</sup>, while nominal solid density of the alloy is 2.68 g/cm<sup>3</sup>.

### 2.2 LPBF System

A Trumpf TruPrint 3000 LPBF system was used in the work (Ditzingen, Germany). The system was equipped with a single-mode fiber laser (RedPower Qube, SPI, Southampton, UK), which operates in continuous wave (CW) emission and 450 W maximum power. The optical system is composed by a dynamic zoom optic and galvanometric mirrors with a nominal minimum beam diameter of 100  $\mu$ m. The build volume is cylindrical with 300 mm diameter and 400 mm maximum build height. Build plate preheating with up to 200 °C can be employed. The LPBF system was operated with N<sub>2</sub>, and the O<sub>2</sub> content is kept under 3000 ppm throughout the build process.

### 2.3 Heat Treatment Systems

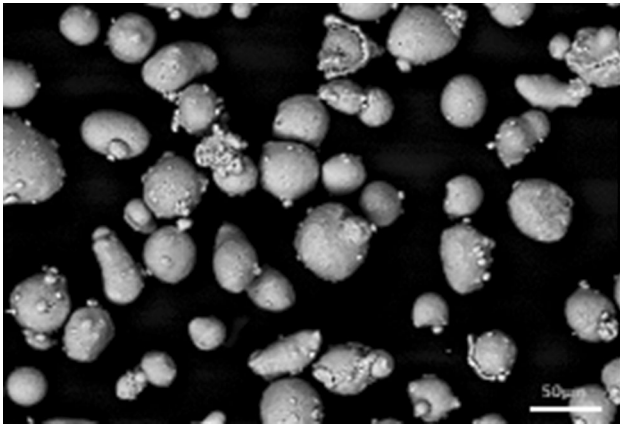
For the heat treatment of the specimens useful for the characterization of the different post-process conditions, two different types of furnaces were used. A Lenton Thermal Design furnace was used for heat treatments in air without the use of an inert gas. The furnace has an internal chamber lined internally with refractory bricks and is equipped with a resistance system controlled by a thermocouple inside the chamber to govern the temperature. A Heraeus Instruments furnace was suitably equipped to work under preheated argon insufflation conditions. The furnace had a process chamber with dimensions 300 mm  $\times$  250 mm  $\times$  400 mm, with a 350 L capacity, lined with refractory material. Inside the treatment chamber a reduced sealed sub-volume has been installed, and constant flow of preheated inert gas was maintained within it, in order to have an inert treatment environment with homogeneous temperature.

### 2.4 Characterization Equipment

Density of the LPBF produced samples was measured based on Archimedes principle (Precisa 100A-300M, Turin, Italy). For the chosen conditions, metallographic cross sections were prepared by cutting and polishing. Optical microscopy images were recorded (Mitutoyo Quick Vision ELF QV-202, Kanagawa, Japan), and apparent density was calculated by image processing software as the fraction of the total area of the pores over the total area of the deposit. Vickers hardness was

**Table 1 The nominal and measured chemical composition of the powder feedstock**

Wt.%	Mg	Si	Zn	Ti	O	Mn	Fe	Cu	N	Al
Nominal	0.45-0.60	6.50-7.50	< 0.050	0.04-0.20	< 0.20	< 0.030	< 0.10	< 0.050	< 0.20	Bal
Measured	0.45	7.36	0.002	0.08	0.09	0.003	0.08	0.006	< 0.01	Bal

**Fig. 2** Morphology of the AlSi7Mg powder used in the experimental work

measured on samples with sufficiently low porosity, with 5 kg applied load. On selected samples SEM/EDS analysis were performed to well identify microstructural constituents.

Tensile tests were performed with constant strain rate at  $\dot{\epsilon}=2.5 \cdot 10^{-4} \text{ s}^{-1}$  using a hydraulic test machine AST28 at 23 °C and according to the ASTM E8M – 16a.

In order to assess the influence of the heat treatment types on the material equilibrium phase diagram was calculated using the measured chemical composition (JMatPro-V12).

### 3. Experimental Study

#### 3.1 Selection of the LPBF Process Parameters

Different parameter sets were investigated in order to achieve fully dense parts. In particular, the study aimed at defining two sets of process parameters with low and high layer thickness ( $z$ ) values. Layer thickness has a direct impact on the process productivity as higher layer thickness can potentially decrease the recoating time and improve the overall build rate ( $BR$ ). The beam diameter was fixed at 100  $\mu\text{m}$ , while the scan pattern was fixed as meander and 100 °C of build platform preheating was used. The gas speed was found to be adequate at 0.8 m/s, while higher speeds generated powder bed denudation and lower ones an excessive generation of smoke. Laser power ( $P$ ) was varied between 210 and 450 W encompassing between relatively moderate power levels to the maximum one. The scan speed ( $v$ ) was varied between 1000 and 2500 mm/s. The hatch distance ( $h$ ) was varied between 0.08 and 0.20 mm corresponding to values smaller and higher than the employer laser beam diameter. Layer thickness was varied at two discrete

**Table 2 Investigated parameter ranges in the experimental work for the selection of the LPBF process parameters**

Fixed factors	Value
Beam diameter, $d_s$ ( $\mu\text{m}$ )	100
Gas speed, $v_g$ (m/s)	0.8
Scan pattern	Meander
Build platform preheating	100 °C
Variable factors	Levels
Power, $P$ (W)	210-450
Scan speed, $v$ (mm/s)	1000-2500
Hatch distance, $h$ (mm)	0.08-0.20
Layer thickness, $z$ (mm)	0.03; 0.05

levels at 30  $\mu\text{m}$  and 50  $\mu\text{m}$  corresponding to higher detail and higher productivity conditions, respectively. The density of all samples was analyzed by the Archimedes method. The experimental conditions are summarized in Table 2. Selected samples were also further analyzed by taking cross sections to reveal the internal porosity.

The results were evaluated as a function of the energy density ( $E$ ) parameter as given by the following equation.

$$E = \frac{P}{z \cdot h \cdot v} \quad (\text{Eq 1})$$

While the energy density is a compound parameter gathering all the main process parameters, the results were grouped as a function of the layer thickness to choose an appropriate condition for the consecutive stages using the two levels of layer thickness. The productivity of the chosen conditions was also evaluated by calculating the theoretical build rate ( $BR$ ) as given by the following equation (Ref 29).

$$BR = z \cdot h \cdot v \quad (\text{Eq 2})$$

It should be noted that the theoretical build rate does not consider the jumps between consecutive scan vectors and parts as well as border scans.

Selected conditions for each layer thickness were further evaluated. For the heat treatment study, cylindrical samples with  $\varnothing 10 \text{ mm} \times 100 \text{ mm}$  dimension and cubic samples with  $5 \times 5 \times 5 \text{ mm}^3$  were produced. The cylindrical samples were machined to the final geometry of done bone specimens with  $\varnothing 6 \text{ mm}$  diameter at the calibrated region. The cubic samples were used for microstructural and hardness analysis. Figure 3 shows the images of cylindrical bars and cubes samples produced in two different layer thicknesses.

### 3.2 Heat treatment Study

The heat treatment study was aimed to investigate an appropriate recipe for small to medium sized bulky parts to be used in railways applications also taking productivity and economical concerns into account. The effect of environment was investigated by carrying out the heat treatments in air and under argon. The argon atmosphere in the furnace for heat treatment can be advantageous for limiting oxide formation on component surface. On the other side, heat treatments performed in air are less costly, in terms of both inert heat treatment furnace cost and gas price. From the point of view of investment costs, an air treatment furnace costs about a quarter of an inert treatment furnace.

Based on the state of the art on heat treatment for aluminum AM components, the first selected condition was the standard T6 heat treatment. This condition has been used as benchmark, to compare the mechanical properties of the sample produced in this campaign with literature data. Two additional heat treatments were applied, modifying the temperature of the isothermal holding of the solution annealing step and/or removing it completely from the process. The new treatments have been designed aiming to maintain similar or improved mechanical characteristics compared to the results achievable with standard T6 (particularly tensile strength and the elongation) (Ref 30, 31). The process steps for each heat treatments are described as follows.

1. Standard T6: This treatment is typically used for conventional cast products and consist of solution annealing followed by aging. It causes in the LPBF materials, the

coarsening of eutectic silicon particles. The solution annealing was carried out at 540 °C for 30 mins followed by fast quenching in water. The aging stage was carried out at 165 °C for 6 h followed by cooling in air.

2. Modified T6: This heat treatment was defined aiming to reduce the coarsening of Si particles. In this case, the T6 treatment solution annealing was applied at a lower at 400 °C for 30 min followed by fast quenching in water. The aging stage was at 165 °C for 6 h followed by cooling in air. This treatment was carried out only under Ar.
3. Direct aging: This heat treatment was defined to understand the effect of avoiding the first phase of T6 standard related to solution annealing and quenching treatment phase. In fact, for bulky parts the use of water quenching can be problematic overall. The cooling rates can be different between the larger and thinner regions generating possible stress and distortions, geometrical deviations and ruptures during quenching. The direct aging treatment was applied at 165 °C for 6 h followed by cooling in air, removing the solution annealing stage.

The heat treatments were applied to LPBF produced samples with two parameter sets using low and high levels of layer thickness. Heat treatments were applied under Ar and in air. The experimental conditions are summarized in Table 3. Microstructures and tensile properties have been evaluated on materials in the tree different heat treatment conditions. For comparison, the as-built conditions were also analyzed. Each condition was tested with three replications.

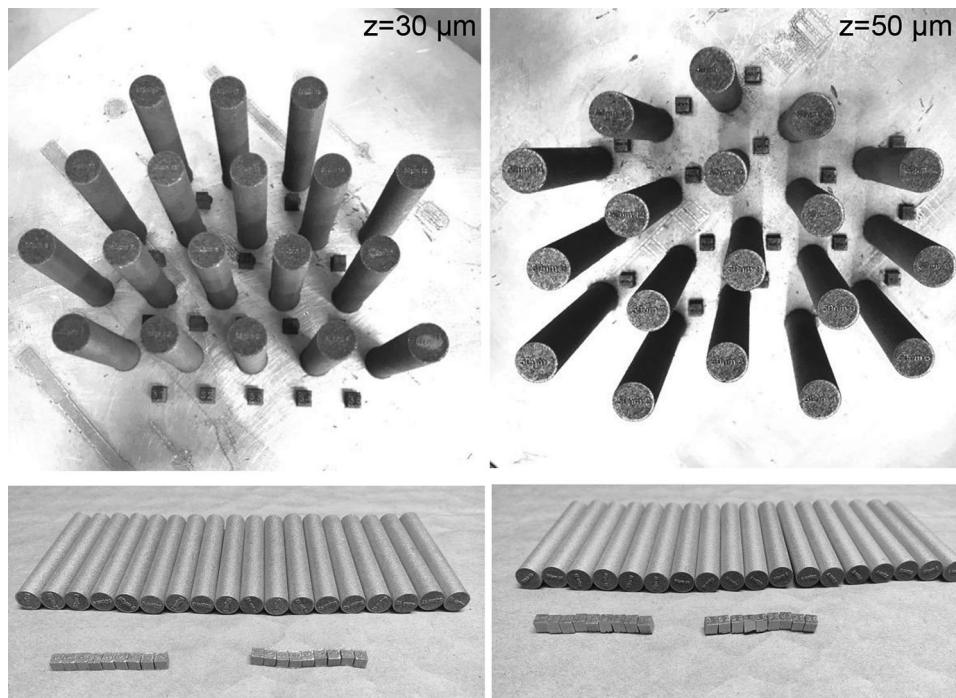


Fig. 3 Samples for the material characterization produced with different layer thicknesses

**Table 3 Fixed and variable factors of experimental campaign**

Variable parameters	Levels
LPBF parameter set	Low $z = 30 \mu\text{m}$ High $z = 50 \mu\text{m}$
Heat treatment atmosphere	Air Ar
Heat treatment type	Standard T6 Modified T6 Direct aging

## 4. Results

### 4.1 Selection of the Process Parameters for the Reduction of the Part Porosity

The measured Archimedes density values of the specimens as a function of energy density grouped for the different layer thickness levels are shown in Fig. 4. In the experiments, the resultant energy density values ranged between 18 and 113 J/mm<sup>3</sup>. The data follow the common increasing density, plateau region and a decaying behavior as the energy density progressively increases (Ref 32). The measured data have a rather large dispersion around the higher values of energy density due to keyhole porosity, which has been previously observed with AlSi7Mg (Ref 16). Moreover, the measured density values are between 2.46 and 2.65 cm<sup>3</sup>/g. Between approximately 38 and 64 J/cm<sup>3</sup>, the density levels saturate around 2.65 cm<sup>3</sup>/g for both of the layer thickness levels, reaching up to approximately 99% of the nominal density. The main causes of porosity are expected to be the lack of fusion (at lower energy density levels) and keyhole porosity (at higher energy density levels). Such plateau regions commonly correspond to the maximum density values reachable for a given material close to a full densification. While the density values are commonly compared to a nominal one, providing a percentage may be misleading due to the variations in the final chemical composition.

Two conditions at 30 and 50  $\mu\text{m}$  layer thicknesses were identified in the plateau region as shown in Table 4. The parameter sets corresponded to the same laser power ( $P = 345$  W), scan speed ( $v = 1500$  mm/s), and hatch distance ( $h = 0.12$  mm). The energy densities were 64 and 38 J/mm<sup>3</sup>, while the build rates were 19 and 32 cm<sup>3</sup>/h for 30  $\mu\text{m}$  and 50  $\mu\text{m}$  layer thicknesses, respectively. These conditions were found suitable for the comparative analysis employing different layer thicknesses, which are summarized in Table 4. The chosen parameter sets were also assessed through the cross-section analysis, and the porosity was analyzed through optical microscopy analysis. The apparent density was found to be higher than 99% for both the conditions as reported in Fig. 5. Therefore, it can be concluded that the chosen conditions are suitable for manufacturing parts with good mechanical properties. These conditions were used in the heat treatment study.

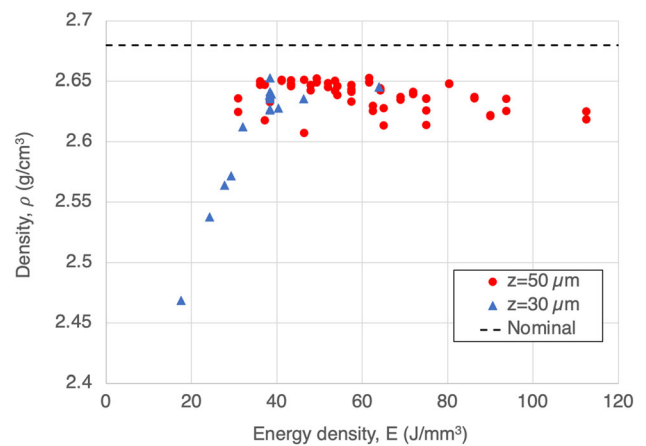


**Fig. 4** Measured Archimedes density of the specimens as a function of energy density grouped for different layer thicknesses

**Table 4** The chosen parameter sets for the heat treatment studied

Parameter	Low $z$	High $z$
Layer thickness, $z$ , $\mu\text{m}$	30 $\mu\text{m}$	50 $\mu\text{m}$
Power, $P$ , W	345	345
Scan speed, $v$ , mm/s	1500	1500
Hatch distance, $h$ , mm	0.12	0.12
Energy density, $E$ , J/mm <sup>3</sup>	64	38
Build rate, $BR$ , cm <sup>3</sup> /h	19	32
Archimedes density, $\rho$ , g/cm <sup>3</sup>	$2.645 \pm 0.004$	$2.634 \pm 0.001$
Optical apparent density, $\rho_A$	99.3%	99.1%

### 4.2 Effect of Heat Treatment on the Material Properties

**4.2.1 Material Microstructure.** The evolution of the as-built microstructure as consequence of the different heat treatments applied in Ar is reported in Fig. 6. Similar microstructures were observed in air. Concerning the as-built sample the eutectic interdendritic silicon particles are well evident. In Fig. 6, the microstructure of aged T6 type samples is shown, where the solidification structure is fully disappeared. Standard T6 treatment causes a coarsening of Si particle (white particles) which reaches size up to 2-5  $\mu\text{m}$ . The EDS analysis shows a Si-enrichment higher than 60%. Modified T6 treatment seems less effective in terms of Si particle coarsening, being the size of these light particles lower than 0.5  $\mu\text{m}$ . The enrichment of Si evaluated by EDS analysis was up to 10-15%, since the analysis is affected by the matrix contribution. However, in modified T6 sample the presence of a second type of precipitate is observable, which are too small to be identified by EDS analysis. It can be supposed that the precipitation of Mg-rich phase starts during solution treatment, and it is completed during aging, producing coarser precipitates respect to those are obtained in standard T6 treatment. On the other hand, the direct

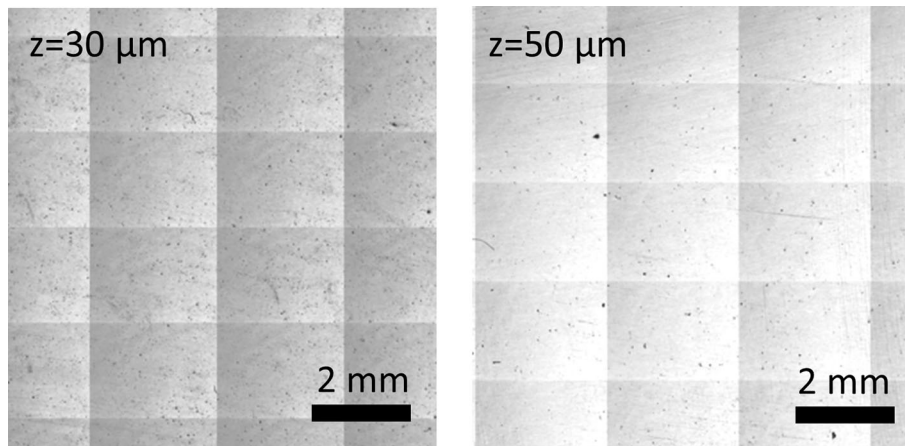


**Fig. 5** The chosen conditions for the heat treatment studies obtained with  $P = 345$  W,  $h = 0.12$  mm,  $v = 1500$  mm/s with variable layer thickness.

aging treatment does not destroy the solidification microstructure, allowing the precipitation of very fine precipitates inside the dendritic spaces. The composition of these particles, presumably Mg-rich precipitates, was not revealable by EDS probe, due to their very fine size.

**4.2.2 Microhardness.** Figure 7 shows the measurements of the microhardness samples produced in different conditions. It can be observed that the hardness was not substantially affected by the layer thickness as well as by the protective gas used in the heat treatment. Direct aging allows to obtain higher hardness values with respect to all the other conditions, as-built sample and heat treatments. The two different T6 heat treatments led to a reduction in hardness compared to the as-built conditions.

**4.2.3 Tensile Properties.** Figure 8 compares the mechanical properties of the materials in the different heat treatment conditions and different layer thicknesses. Figure 8a depicts the ultimate tensile strength. As-built specimens made by with  $30 \mu\text{m}$  layer thickness have higher tensile strength. This phenomenon is probably related to the number of material thermal cycles, which results in higher work hardening with lower layer thickness. Regarding the effects of the different atmospheres, there are no significant differences between the use of air and argon. The oxidation, limited to the surface layer of the samples, is removed from the sample during the sample machining, and the sublayers have a microstructure depending only by the heat treatment conditions. Aluminum alloys in fact, although easily oxidizable, form a passivating compact layer of oxide on the surface that does not allow oxygen in the air to penetrate and therefore the oxidation stops at a layer of a few microns thickness. It can be observed that the T6 treatments reduce the tensile strength compared to the as-built conditions, and the effect is higher for the modified treatment. On the other side, the direct aging allows to obtain higher tensile strengths with respect to all the other conditions, as-built sample, and other heat treatments. The yield strengths show the same trend of hardness and ultimate tensile strength (Fig. 8b) showing that the highest value is obtained by direct aging. The standard T6 condition generally increases the yield strength with respect to as-built and T6 modified treatment.

The as-built samples show relatively low ductility, which can be associated with the hardening caused by the rapid solidification occurring in the LPBF process. The effects of this

phenomenon can be mitigated by heat treatments that reduce internal stresses in the material. This behavior is confirmed by the results obtained in this work. It can be observed in Fig. 8c that the elongation is generally increased by all the treatments and the effect is higher for both the T6 treatments. The maximum elongation increase was obtained using the modified T6 treatment.

Elastic moduli are shown in Fig. 8d. for all the tested conditions. A general increase of the elastic modulus values is obtained by the heat treatments. The maximum increase, compared to the as-built conditions, was achieved for the direct aging treatment. No variations were noted for the different LPBF process conditions or for the use of the standard or modified T6 treatment.

## 5. Discussion

The aim of this study was to investigate how different heat treatments lead to different mechanical behavior giving the key to achieve the target properties of the final component operating in different application sectors. In the case of the project in question, for components to be used in the railway sector, the aim is to obtain good mechanical properties such as high yield strength, low deformations and fatigue resistance. Taking into consideration also a possible industrialization of the component obtained through additive manufacturing, it has been investigated also the possibility of carrying out treatments in air rather than in more expensive inert gases such as argon, or to avoid water quenching treatments for complex components, which could lead to local deformations. The effect of layer thickness on the final properties has been also evaluated, considering that large layer thickness has a positive impact on production rate.

In order to better understand the effect of the heat treatments, an equilibrium phase diagram was calculated as seen in Fig. 9. The heat treatment conditions modify the hardened solidification microstructure of the as-built materials, and, as consequence, influence the mechanical properties. The first effect is to reduce the hardening level, reducing residual stresses and dislocation density, with a general increase of the material ductility. The modified T6 treatment condition determines, as for the standard treatment, the almost complete

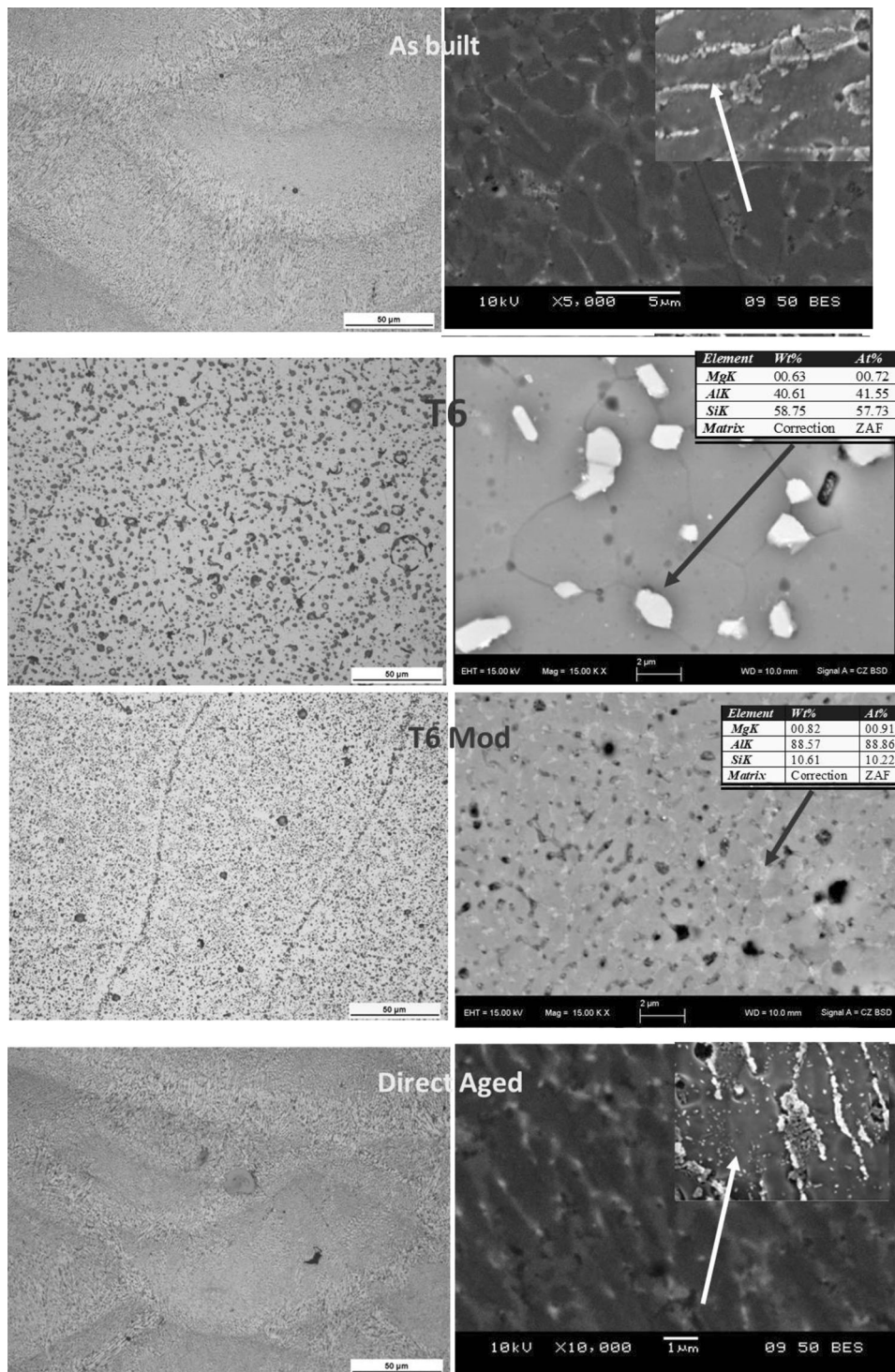


**Fig. 6** Comparison of microstructures of samples produced in different heat treatment conditions applied under argon

disappearance of the original solidification microstructure, with a more limited coarsening of the Si eutectic particles formed during the solidification process. However, at the selected temperature of 400 °C, the Mg-Si intermetallic phase is stable, since it is formed for temperature lower than 490 °C, as predicted by the equilibrium phase diagram. As consequence, this phase starts to precipitate during solution step, producing a coarser distribution which is less effective in the improving the material strength. The direct aging, conducted at 165 °C for 6

hours, allows to reduce the residual stress and hardening level of the as-built material, without affecting the Si particle size. On the other side, this treatment is suitable to produce a fine intermetallic precipitation with a positive effect on both the material strength and the ductility.

Overall, the results show that high productive LPBF process with a larger layer thickness ( $z = 50 \mu\text{m}$ ) can be employed combined with a direct aging treatment in air. In combination an economically more viable process and shorter cycle time is

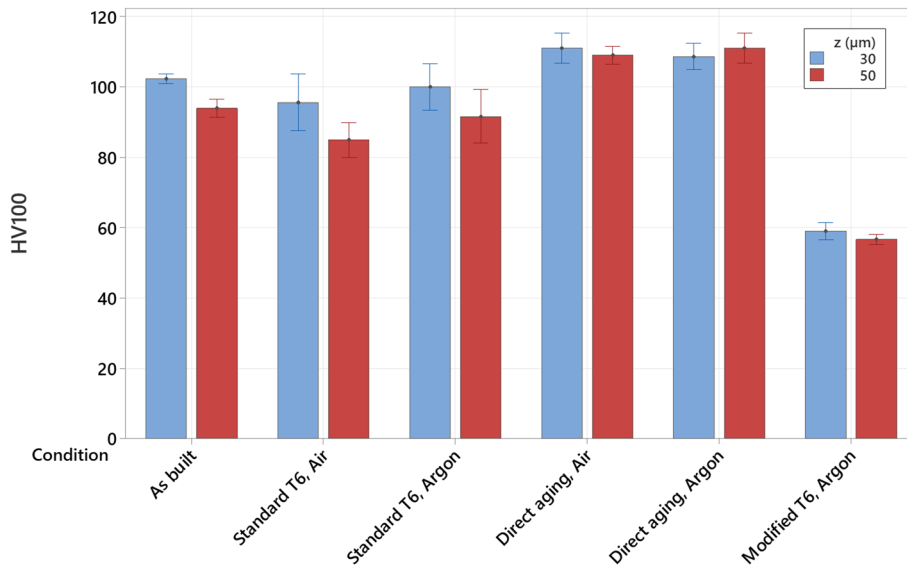
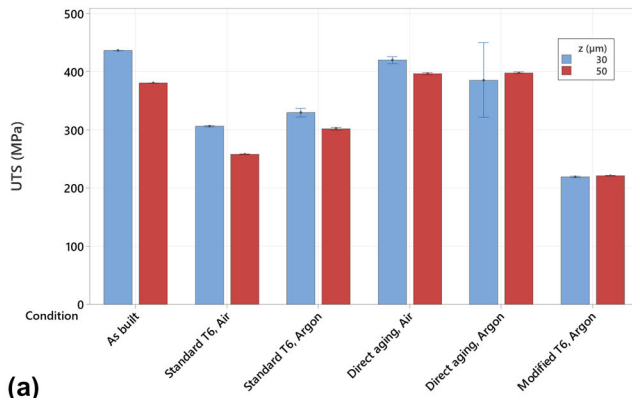
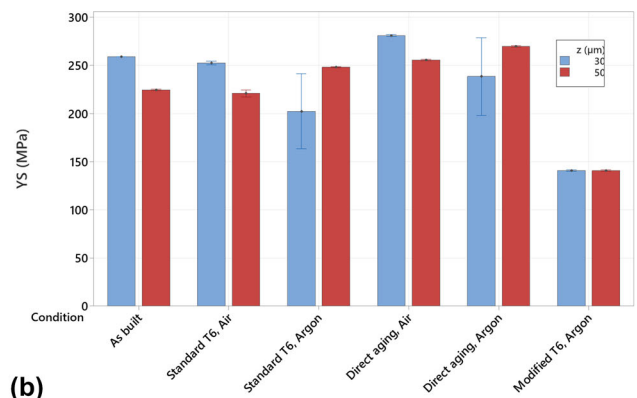


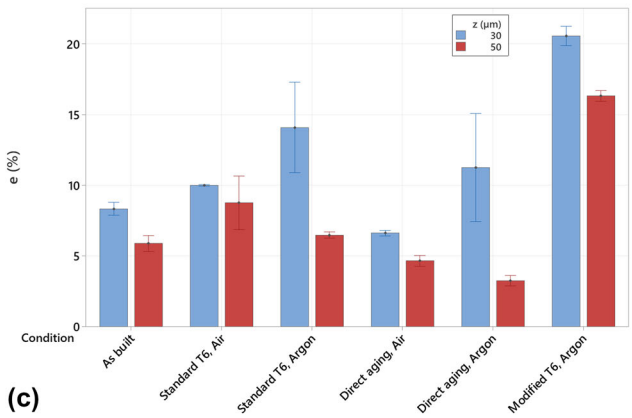
**Fig. 7** Vickers hardness measurements of the as-built and heat-treated specimens



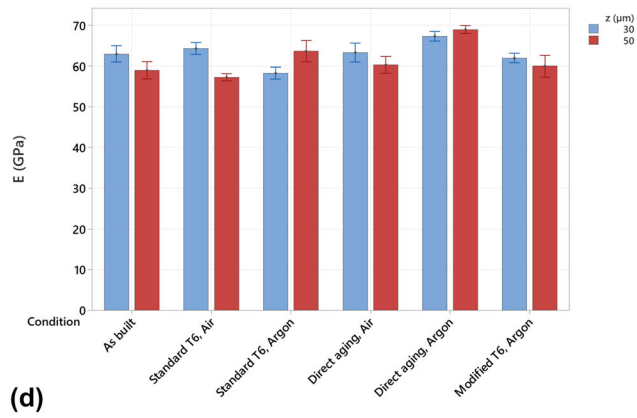
**(a)**



**(b)**



**(c)**



**(d)**

**Fig. 8** Tensile strength measurements of the as-built and heat-treated specimens

determined to be useful for the application requirements. Although the static tensile properties tested here are indicative toward also the fatigue behavior, more studies are required on the matter. The LPBF process applied at low layer thickness upon direct aging provides a higher elongation, which may also be beneficial for avoiding a fragile behavior toward a better

fatigue resistance. Another important factor remains the corrosion properties, which was not the main concern of this study. In summary, the proposed manufacturing cycle can be readily used for parts that are not safety critical. The use of painting and coating stages can be also assessed for corrosion protection depending on the application area of the component.



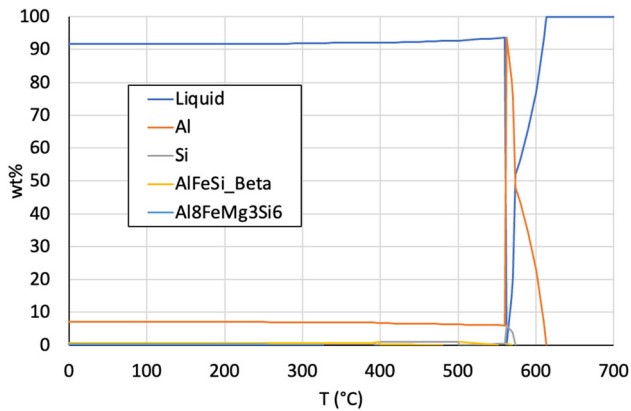


**Fig. 9** Equilibrium phase diagram calculated by JMatPro-V12 for Al-0.08Fe-0.45 Mg-7.36Si-0.08Ti-0.002Zn wt.%

## 6. Conclusions

This work showed a systematic analysis of an additive manufacturing cycle for railways industry. The AlSi7Mg alloy was processed by LPBF, and different heat treatment conditions were analyzed seeking a solution adaptable to spare part manufacturing in a decentralized manner. This confirmed that the Al-alloys used with the LPBF technology can provide a valid option for spare part manufacturing based on digital data. The Al alloy can be processed at relatively high build rates and combined with tailored heat treatments to achieve desirable mechanical properties. The results showed that a direct aging treatment was able to maintain the solidification structure without compromising extensively the highly strong microstructure achieved during the additive manufacturing phase. The impact of the final additive manufacturing route on the fatigue properties as well as the corrosion resistance remains open points for future investigations.

## Acknowledgments

This work was carried out under the project “NEXT generation of methods, concepts and solutions for the design of robust and sustainable running GEAR (NEXTGEAR)” funded by the European Union’s Horizon 2020 research and innovation programme under grant agreement No: 881803.

## Funding

Open access funding provided by Politecnico di Milano within the CRUI-CARE Agreement.

## Open Access

This article is licensed under a Creative Commons Attribution 4.0 International License, which permits use, sharing, adaptation, distribution and reproduction in any medium or format, as long as you give appropriate credit to the original author(s) and the source, provide a link to the Creative Commons licence, and indicate if changes were made. The images or other third party material in this article are included in the article’s Creative Commons licence, unless indicated otherwise in a credit line to the material. If material is

not included in the article’s Creative Commons licence and your intended use is not permitted by statutory regulation or exceeds the permitted use, you will need to obtain permission directly from the copyright holder. To view a copy of this licence, visit <http://creativecommons.org/licenses/by/4.0/>.

## References

1. H. Fu and S. Kaewunruen, State-of-the-Art Review on Additive Manufacturing Technology in Railway Infrastructure Systems, *J. Compos. Sci.*, 2022 <https://doi.org/10.3390/jcs6010007>
2. S.H. Khajavi, J. Partanen, and J. Holmström, Additive Manufacturing in the Spare Parts Supply Chain, *Comput. Ind.*, 2014, **65**, p 50–63. <https://doi.org/10.1016/j.compind.2013.07.008>
3. R. Muvunzi, K. Mpofu, I. Daniyan, and F. Fameso, Analysis of Potential Materials for Local Production of a Rail Car Component Using Additive Manufacturing, *Heliyon*, 2022, **8**, p e09405. <https://doi.org/10.1016/j.heliyon.2022.e09405>
4. Z. Wu, S. Wu, W. Qian, H. Zhang, H. Zhu, Q. Chen, Z. Zhang, F. Guo, J. Wang, and P.J. Withers, Structural Integrity Issues of Additively Manufactured Railway Components: Progress and Challenges, *Eng. Fail. Anal.*, 2023, **149**, p 107265. <https://doi.org/10.1016/j.engfailanal.2023.107265>
5. A.D. Toth, J. Padayachee, T. Mahlatji, and S. Vilakazi, Report on Case Studies of Additive Manufacturing in the South African Railway Industry, *Sci. Afr.*, 2022 <https://doi.org/10.1016/j.sciaf.2022.e01219>
6. A. Killen, L. Fu, S. Coxon, R. Napper, Exploring the use of additive manufacturing in providing an alternative approach to the design, manufacture and maintenance of interior rail components, in *Proceedings of Australasian Transport Research Forum (ATRF 2018)*, pp 1–16 (2018)
7. P. Kingsland, 3D printing in the railway sector with Deutsche Bahn, *Railw. Technol.* (2019)
8. E. Maleki, S. Bagherifard, M. Bandini, and M. Guagliano, Surface Post-Treatments for Metal Additive Manufacturing: Progress, Challenges, and Opportunities, *Addit. Manuf.*, 2021, **37**, p 101619. <https://doi.org/10.1016/j.addma.2020.101619>
9. J. Fiocchi, A. Tuissi, and C.A. Biffi, Heat Treatment of Aluminium Alloys Produced by Laser Powder Bed Fusion: A Review, *Mater. Des.*, 2021 <https://doi.org/10.1016/j.matdes.2021.109651>
10. K.G. Prashanth, S. Scudino, H.J. Klauss, K.B. Surreddi, L. Löber, Z. Wang, A.K. Chaubey, U. Kühn, and J. Eckert, Microstructure and Mechanical Properties of Al-12Si Produced by Selective Laser Melting: Effect of Heat Treatment, *Mater. Sci. Eng. A*, 2014, **590**, p 153–160. <https://doi.org/10.1016/j.msea.2013.10.023>
11. J.L. Bartlett, and X. Li, An Overview of Residual Stresses in Metal Powder Bed Fusion, *Addit. Manuf.*, 2019, **27**, p 131–149. <https://doi.org/10.1016/j.addma.2019.02.020>
12. R. Sorci, O. Tassa, A. Colaneri, A. Astri, D. Mirabile, S. Iwnicki, and A.G. Demir, Design of an Innovative Oxide Dispersion Strengthened Al Alloy for Selective Laser Melting to Produce Lighter Components for the Railway Sector, *J. Mater. Eng. Perform.*, 2021, **30**, p 5184–5194. <https://doi.org/10.1007/s11665-021-05693-5>
13. L. Girelli, M. Tocci, L. Montesano, M. Gelfi and A. Pola, Optimization of heat treatment parameters for additive manufacturing and gravity casting AlSi<sub>10</sub>Mg alloy, in *IOP Conference Series: Materials Science and Engineering*, vol. 264. <https://doi.org/10.1088/1757-899X/264/1/012016> (2017)
14. H. Rao, S. Giet, K. Yang, X. Wu, and C.H.J. Davies, The Influence of Processing Parameters on Aluminium Alloy A357 Manufactured by Selective Laser Melting, *Mater. Des.*, 2016, **109**, p 334–346. <https://doi.org/10.1016/j.matdes.2016.07.009>
15. L.Z. Wang, S. Wang, and J.J. Wu, Experimental Investigation on Densification Behavior and Surface Roughness of AlSi<sub>10</sub>Mg Powders Produced by Selective Laser Melting, *Opt. Laser Technol.*, 2017, **96**, p 88–96. <https://doi.org/10.1016/j.optlastec.2017.05.006>
16. T. Kimura and T. Nakamoto, Microstructures and Mechanical Properties of A356 (AlSi<sub>7</sub>Mg<sub>0.3</sub>) Aluminum Alloy Fabricated by Selective Laser Melting, *Mater. Des.*, 2016, **89**, p 1294–1301. <https://doi.org/10.1016/j.matdes.2015.10.065>
17. F. Trevisan, F. Calignano, M. Lorusso, J. Pakkanen, E.P. Ambrosio, L. Mariangela, M. Pavese, D. Manfredi and P. Fino, Effects of heat

- treatments on A357 alloy produced by selective laser melting, in *World PM 2016 Congr. Exhib.* (2016)
18. X. Zhang, J. Kang, Y. Rong, P. Wu, and T. Feng, Effect of Scanning Routes on the Stress and Deformation of Overhang Structures Fabricated by SLM, *Materials (Basel)*, 2018 <https://doi.org/10.3390/ma12010047>
  19. D. Buchbinder, W. Meiners, N. Pirch, K. Wissenbach, and J. Schrage, Investigation on Reducing Distortion by Preheating during Manufacture of Aluminum Components Using Selective Laser Melting, *J. Laser Appl.*, 2014, **26**, p 012004. <https://doi.org/10.2351/1.4828755>
  20. J. Fioocchi, A. Tuissi, P. Bassani, and C.A. Biffi, Low Temperature Annealing Dedicated to AlSi<sub>10</sub>Mg Selective Laser Melting Products, *J. Alloys Compd.*, 2017, **695**, p 3402–3409. <https://doi.org/10.1016/j.jallcom.2016.12.019>
  21. J. Pezda, Optimization of Heat Treatment Parameters of AlSi<sub>7</sub>Mg Alloy, *Materials (Basel)*, 2022, **15**, p 9–12. <https://doi.org/10.3390/ma15031163>
  22. L.F.L. Martins, P.R. Provencher, M. Brochu, and M. Brochu, Effect of Platform Temperature and Post-processing Heat Treatment on the Fatigue Life of Additively Manufactured AlSi<sub>7</sub>Mg Alloy, *Metals (Basel)*, 2021 <https://doi.org/10.3390/met11050679>
  23. J.T.O. de Menezes, E.M. Castrodeza, L. Patriarca, and R. Casati, Effect of Heat Treatments and Loading Orientation on the Tensile Properties and Fracture Toughness of AlSi<sub>7</sub>Mg Alloy Produced by Laser Powder Bed Fusion, *Int. J. Fract.*, 2022, **235**, p 145–157. <https://doi.org/10.1007/s10704-022-00631-5>
  24. T. Zou, M. Chen, H. Zhu, and S. Mei, Effect of Heat Treatments on Microstructure and Mechanical Properties of AlSi<sub>7</sub>Mg Fabricated by Selective Laser Melting, *J. Mater. Eng. Perform.*, 2022, **31**, p 1791–1802. <https://doi.org/10.1007/s11665-021-06324-9>
  25. X. Ming, D. Song, A. Yu, H. Tan, Q. Zhang, Z. Zhang, J. Chen, and X. Lin, Effect of Heat Treatment on Microstructure, Mechanical and Thermal Properties of Selective Laser Melted AlSi<sub>7</sub>Mg Alloy, *J. Alloys Compd.*, 2023, **945**, p 169278. <https://doi.org/10.1016/j.jallcom.2023.169278>
  26. S. Cacace, A.G. Demir, G. Sala, and A.M. Grande, Influence of Production Batch Related Parameters on Static and Fatigue Resistance of LPBF Produced AlSi<sub>7</sub>Mg<sub>0.6</sub>, *Int. J. Fatigue*, 2022, **165**, p 107227. <https://doi.org/10.1016/j.ijfatigue.2022.107227>
  27. M. Vanzetti, E. Virgillito, A. Aversa, D. Manfredi, F. Bondioli, M. Lombardi, and P. Fino, Short Heat Treatments for the F357 Aluminum Alloy Processed by Laser Powder Bed Fusion, *Materials (Basel)*, 2021, **14**, p 6157. <https://doi.org/10.3390/ma14206157>
  28. J.Y. Hu, P. Liu, S.Y. Sun, Y.H. Zhao, Y.B. Zhang, and Y.S. Huo, Relation Between Heat Treatment Processes and Microstructural Characteristics of 7075 Al Alloy Fabricated by SLM, *Vacuum*, 2020, **177**, p 109404. <https://doi.org/10.1016/j.vacuum.2020.109404>
  29. M. Tang, P.C. Pistorius, C. Montgomery, and J. Beuth, Build Rate Optimization for Powder Bed Fusion, *J. Mater. Eng. Perform.*, 2019, **28**, p 641–647. <https://doi.org/10.1007/s11665-018-3647-5>
  30. D.S. MacKenzie, Heat Treatment Practice of Wrought Age-Hardenable Aluminum Alloys, *Alum. Sci. Technol.*, 2018, **2**, p 462–477. <https://doi.org/10.31399/asm.hb.v02a.a0006520>
  31. V.A. Medrano, E. Arrieta, J. Merino, B. Ruvalcaba, K. Caballero, B. Ramirez, J. Diemann, L.E. Murr, R.B. Wicker, D. Godfrey, M. Benedict, and F. Medina, A Comprehensive and Comparative Study of Microstructure and Mechanical Properties for Post-process Heat Treatment of AlSi<sub>7</sub>Mg Alloy Components Fabricated in Different Laser Powder Bed Fusion Systems, *J. Mater. Res. Technol.*, 2023, **24**, p 6820–6842. <https://doi.org/10.1016/j.jmrt.2023.04.129>
  32. H. Hyer, L. Zhou, S. Park, G. Gottsfriz, G. Benson, B. Tolentino, B. McWilliams, K. Cho, and Y. Sohn, Understanding the Laser Powder Bed Fusion of AlSi<sub>10</sub>Mg Alloy, *Metallogr. Microstruct. Anal.*, 2020, **9**, p 484–502. <https://doi.org/10.1007/s13632-020-00659-w>

**Publisher's Note** Springer Nature remains neutral with regard to jurisdictional claims in published maps and institutional affiliations.